PNAS RESEARCH ARTICLE | PLANT BIOLOGY

Single-nucleus and spatial transcriptomics reveal the cell populations of intercalary meristems in bamboo

Ning Qin[a,b,1], Xin Liu[c,d,1], Shanying Li[a,b,1], Lei Sun[a,b,1], Chuan Chen[c,e,1], Wenrui Lou[f], Xianke Wang[g], Pengfei Bao[a,b], Bingchen Cao[a,b], Huan Zhang[a,b], Junwei Gan[a,b], Yinguang Hou[a,b], Zeyu Fan[a,b], Jianlin Liu[c], Yu Wang[d,h], Huanming Yang[d], and Hansheng Zhao[a,b,2]

Affiliations are included on p. 11.

Edited by Julia Bailey-Serres, University of California, Riverside, CA; received May 11, 2025; accepted November 2, 2025

Intercalary meristems (IcMs), specialized developmental zones that drive rapid stem elongation in monocots, exhibit distinct spatiotemporal dynamics; however, their genetic basis remains poorly understood due to their transient activity and cellular heterogeneity. Moso bamboo (*Phyllostachys edulis*)—with its exceptional daily growth rates of up to 114.5 cm, prolonged IcM activity spanning 45 to 60 d, and large, accessible culm structure—provides an ideal system for building a comprehensive IcM cell atlas. Here, we integrated a chromosome-level genome assembly of Moso bamboo with a high-resolution anatomical atlas to delineate three critical developmental stages of IcM activity: the initial cell division phase (ID), the rapid cell division phase (RD), and the rapid cell elongation phase (RE). By combining single-nucleus RNA sequencing (snRNA-seq) and spatial transcriptomics, we reconstructed a dynamic single-nucleus transcriptomic continuum spanning from proliferative to elongation states. Multiomics integration, along with in situ hybridization and ultrastructural imaging, identified IcM cells as short-columnar cells adjacent to elongating ground tissue parenchyma (Gp) cells, with the IcM1 subpopulation functioning as stem-like cells essential for maintaining the proliferative capacity. Pseudotemporal trajectory analysis revealed transcriptional transitions from stem-like IcM states to differentiated Gp cells. Functional experiments revealed that *clrGene008562*, a *WOX2* homolog, enhances callus regeneration, indicating its potential role in promoting cell division and differentiation processes relevant to IcM development. These findings provide a comprehensive molecular and cellular framework for understanding IcM function and offer valuable multiomics resources for advancing meristem research in bamboo and other Poaceae species.

intercalary meristems | Moso bamboo | internode elongation | spatial transcriptome | single-nucleus transcriptome

Significance

Intercalary meristems (IcMs) coordinate rapid stem elongation in monocots, yet their cellular organization and regulatory pathways remain largely uncharacterized due to their transient activity and inaccessibility in typical model species. Moso bamboo offers an unparalleled system for IcM research, combining extraordinary daily growth rates (up to 114.5 cm), prolonged meristematic activity (45 to 60 d), and large culm diameters (8 to 15 cm) that facilitate precise tissue sampling. Our integrated single-nucleus and spatial transcriptomic atlas delineates distinct IcM populations, including highly proliferative short-columnar cells and a stem-like IcM1 subpopulation, charts their developmental dynamics, and uncovers key regulatory networks. These findings provide fundamental insights into meristematic biology with transformative implications for enhancing crop productivity and developing sustainable biomaterial resources.

Intercalary meristems (IcMs) are specialized types of primary meristems that are strategically localized within discrete tissue zones and serve as pivotal regulators of internode elongation in Poaceae species, such as rice, maize, and bamboo (1–4). Unlike apical or lateral meristems, including the shoot apical meristem (SAM), IcMs are characterized by a unique structural organization and finely tuned spatiotemporal regulation of cellular processes, coordinating cell division, expansion, and differentiation within confined developmental domains. This coordination plays a critical role in shaping plant architecture and underlies the rapid elongation of stems and leaves (5). The spatial precision and activity of IcMs directly impact key agronomic traits such as culm height and mechanical strength, both critical for biomass accumulation and structural integrity (3, 6). Despite their biological and agricultural importance, the molecular mechanisms governing IcM identity, developmental trajectories, and regulatory network dynamics remain largely unexplored (4, 7). While studies in cereal crops such as rice and maize have provided initial insights into IcMs (2, 3, 8), these model systems typically lack the extended activity period and spatial accessibility necessary for dissecting the dynamic transitions and regulatory programs that define IcM function over developmental time.

Moso bamboo (*Phyllostachys edulis*), a giant timber grass native to China (9) and the fastest-growing plant on Earth (10), has emerged as a compelling candidate for IcM research; its IcM-driven arborescent growth supports record-breaking elongation rates of up to 114.5 cm d^{-1} (11), enabling the development of towering culms that can reach 25 m in height and 18 cm in diameter. Notably, Moso bamboo maintains active IcMs for 45 to 60 d, providing an extended temporal window for investigating developmental transitions and meristematic regulation (12). Anatomical analyses have revealed a clear developmental gradient within IcM regions, transitioning from zones of intense cell division to areas dominated by cell elongation (11, 13). This progression is tightly regulated

The authors declare no competing interest.

This article is a PNAS Direct Submission.

[1]N.Q., X.L., S.L., L.S., and C.C. contributed equally to this work.

[2]To whom correspondence may be addressed. Email: zhaohansheng@icbr.ac.cn.

This article contains supporting information online at https://www.pnas.org/lookup/suppl/doi:10.1073/pnas.2511701122/-/DCSupplemental.

Published December 18, 2025.

by hormones, particularly the antagonistic interaction between auxin and cytokinin, which governs the transition from proliferation to elongation (11). Additionally, gibberellins facilitate rapid cell elongation by activating cell wall-loosening enzymes, such as *EXPA1* and *EXPA4* (11, 14, 15), which are involved in maintaining stem cell identity. In contrast, abscisic acid (ABA) has been shown to suppress meristematic activity by inhibiting cell cycle regulators and interfering with auxin signaling, while low ABA levels are essential for maintaining quiescent center identity and preventing premature differentiation (16, 17). Molecular studies have further implicated conserved regulators of stem cell identity, including the *WUSCHEL* (*WUS*) gene family, in maintaining meristematic identity and function (18). However, the field continues to face challenges, as cellular heterogeneity and the limitations of bulk tissue analyses hinder the resolution of cell type–specific dynamics, thereby restricting a comprehensive understanding of IcM function and regulation.

A central challenge in the study of IcMs is the accurate identification of IcM cell populations and the capture of their dynamic molecular states, as these cells are deeply embedded within surrounding mature tissues. Traditional bulk omics approaches lack the resolution to resolve IcM-specific molecular signatures, as they average signals across heterogeneous cell populations, obscuring critical spatial and temporal expression dynamics (19). However, recent advances in spatial multiomics technologies, such as single-nucleus RNA sequencing (snRNA-seq) and spatial transcriptomics (ST), have enabled high-resolution characterization of rare and novel cell types, reconstruction of pseudotemporal trajectories, and resolution of spatiotemporal gene expression gradients (20). In nonmodel plants such as bamboo, the integration of these technologies with anatomical imaging and machine-learning-driven cell segmentation has provided unprecedented insights into the identity, spatial organization, and functional specialization of IcM cell populations (4).

In this study, we present an integrative framework that combines an updated chromosome-scale genome of Moso bamboo, high-resolution anatomical and ultrastructural atlases, and comprehensive single-nucleus and spatial transcriptomic profiles across three developmental stages to systematically identify IcM-specific cell populations and elucidate their functional roles. By combining spatially enhanced resolution omics sequencing (Stereo-seq), snRNA-seq, and an autofluorescence-based segmentation pipeline, we resolved IcM populations at single-cell resolution, delineated their spatial zonation, and reconstructed developmental trajectories that govern the transition from cell proliferation to elongation. Spatially resolved in situ hybridization (ISH) and functional experiments demonstrated that cell type–specific marker genes and key transcriptional regulators orchestrate the maintenance of stem cell identity in Moso bamboo. To facilitate further exploration, we developed an interactive web atlas (https://db.cngb.org/stomics/datasets/STDS0000377), providing access to these multiomics resources and facilitating dynamic exploration of IcM regulatory networks. Therefore, this work advances our understanding of the genetic and developmental mechanisms underlying IcM plasticity and the remarkable growth dynamics of bamboo, while providing valuable insights into IcM regulation across Poaceae species.

Results

Anatomical and Physiological Characterization of IcM Regions. To resolve IcM cell populations at single-cell resolution, we constructed an anatomical atlas of IcM regions spanning three developmental stages: the initial cell division phase (ID), the rapid cell division phase (RD), and the rapid cell elongation phase (RE) (Fig. 1 and *SI Appendix*, Fig. S1). To support the subsequent multiomics analyses, we generated a high-quality, chromosome-level reference genome from the single clonal individual used in all experiments, drawing upon prior experience in bamboo genome assembly (21–23), and thereby establishing a solid foundation for all genomic and transcriptomic analyses (*SI Appendix*, Tables S1–S15).

Histological profiling with Safranin O-Fast Green staining revealed a clear developmental transition. The nuclear density was significantly greater during the ID and RD phases than during the RE phase (two-way ANOVA, Tukey's test, $P < 7.27 \times 10^{-17}$), whereas the luminal diameter of the cells was significantly greater in the RE stage (two-way ANOVA, Tukey's test, $P < 3.82 \times 10^{-14}$) (Fig. 2 *A* and *B*). Additionally, the cellulose and lignin contents were significantly greater in the RE phase than in the ID phase (two-way ANOVA, Tukey's test, $P < 9.00 \times 10^{-3}$) (Fig. 2 *C* and *D*). Hormone profiling further supported these developmental transitions: ABA levels were significantly lower in the RD phase than in the ID and RE phases (two-way ANOVA, Tukey's test, $P < 0.029$), whereas auxin (IAA), cis-zeatin (CZ), and trans-zeatin (TZ) concentrations peaked during the ID phase (Fig. 2 *E*–*H*). Together, these findings delineate a clear developmental transition from proliferation-dominant states in the ID and RD phases to an elongation-dominant state during the RE phase.

In addition, to achieve high-resolution cell contour segmentation, we utilized the intrinsic autofluorescence of Moso bamboo cell walls (excitation wavelength: 350 to 400 nm), generating label-free, single-cell-level resolution images that delineated individual cell boundaries (Fig. 2*I* and *SI Appendix*, Fig. S2). We then applied a pretrained CellPose model (24), which was optimized using our autofluorescence dataset, to accurately segment the cell contours across different developmental phases (Fig. 2*J*). Based on histomorphology criteria (25, 26), we manually classified IcM region cells into 12 anatomically distinct cell types (Fig. 2 *K* and *L* and *SI Appendix*, Table S16). This anatomically resolved framework, which connects cellular morphology with spatial positioning, provides a critical foundation for integrating these cell type identities with their corresponding transcriptomic datasets in subsequent analyses.

Spatial and Single-Nucleus Transcriptomic Dissection of IcM Region Cell Populations. We constructed a spatial transcriptomics atlas of the IcM region using Stereo-seq, resolving its cellular composition at single-cell transcriptomic resolution. We primarily utilized a bin100 resolution (50 × 50 μm), as both previous studies (4, 27) and our evaluation confirmed this provided an optimal balance between spatial precision and transcriptomic depth (*SI Appendix*, Figs. S3 and S4 and Table S17). The spatial transcriptomics atlas captured 15,570 to 21,497 bins across developmental stages (Fig. 3 *A* and *B* and *SI Appendix*, Fig. S5 and Table S17). The median gene number per bin ranged from 1,190 to 1,804, with over 37,000 genes detected per stage (*SI Appendix*, Fig. S5 and Table S17). Comparative assessments further showed that the RD bin100 dataset provided the sharper tissue-domain boundaries and higher concordance with anatomical annotations (Jaccard index = 88.7%) (Fig. 3 *C* and *D* and *SI Appendix*, Fig. S6). Thus, we performed unsupervised clustering on the RD phase dataset, which identified seven spatiotemporally distinct spatial clusters (spClusters), with sizes ranging from 169 bins (spCluster-6) to 6,940 bins (spCluster-0) (Fig. 3*A* and *SI Appendix*, Table S18). Highly expressed genes were identified for each spCluster from the bin100 dataset (Fig. 3*B* and *SI Appendix*, Figs. S7 and S8 and Table S19). To annotate these spClusters, we

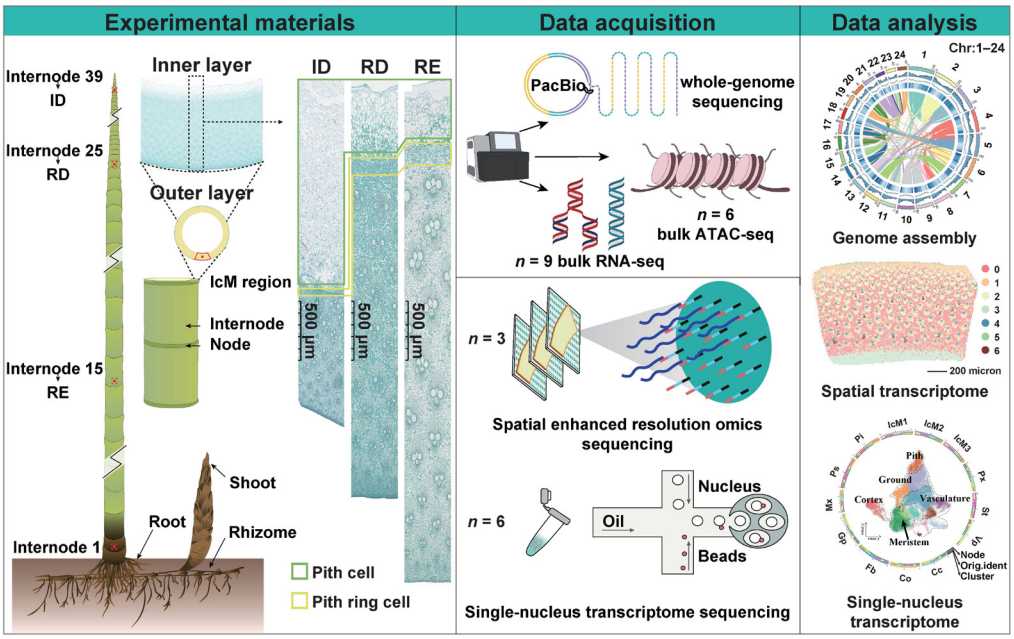

Fig. 1. Integrated multiomics workflow revealing the spatiotemporal dynamics of Moso bamboo intercalary meristem (IcM) regions. This figure illustrates the sampling strategy and multiomics framework designed to investigate the spatiotemporal dynamics of IcM region cells across three developmental stages. IcM regions were sampled from three distinct internodal positions, each representing a different developmental stage. The ID (initial division, 39th internode) stage involves sampling the full internode, which is characterized by moderate nuclear occurrence and is indicative of early mitotic activity and minimal elongation. At the RD (rapid division, 25th internode) stage, a 0.5 cm segment above the node was sampled, which presented peak nuclear density, the highest mitotic index, and intermediate cell length. The RE (rapid elongation, 15th internode) stage was defined by sampling a 0.5 cm segment above the node, which displayed maximal elongation and reduced nuclear content. The three representative developmental stages represented the transition from division to elongation. High-resolution sequencing technologies, including spatially enhanced resolution omics sequencing (Stereo-seq), single-nucleus RNA-seq (snRNA-seq), PacBio-seq, bulk RNA-seq, and bulk ATAC-seq, have been integrated to achieve comprehensive multiomics characterization.

aligned the spClusters to anatomically defined zones, achieving a high degree of spatial concordance (Jaccard index = 88.7%) (Fig. 3 *C* and *D*). Based on this alignment, the spClusters were annotated as follows: ground parenchyma zones (spCluster-0), unclassified zones (spCluster-1), fiber zones (spCluster-2), pith zones (spCluster-3), phloem zones (spCluster-4), cortex zones (spCluster-5), and xylem zones (spCluster-6).

We also performed snRNA-seq with two biological replicates at each developmental stage. After data quality control and batch correction, we retained 128,370 high-confidence nuclei with 51,318 detected genes, covering 96.64% of the annotated genes (*SI Appendix*, Table S20). The median number of detection metrics per nucleus was 2,504 unique molecular identifiers (UMIs) and 1,479 detected genes (*SI Appendix*, Table S20). We identified 13 distinct single-nucleus clusters (snClusters), with sizes ranging from 786 nuclei (snCluster-12) to 26,858 nuclei (snCluster-0) (Fig. 3*E* and *SI Appendix*, Table S21). UMAP embeddings revealed that all six snRNA-seq libraries and all 13 snClusters were consistently represented across developmental stages and replicates (*SI Appendix*, Figs. S9 and S10). Several snClusters exhibited dynamic abundance changes during development (*SI Appendix*, Fig. S11). Additionally, the snRNA-seq dataset exhibited high biological reproducibility across replicates (Pearson's $r > 0.98$) and was strongly correlated with bulk RNA-seq profiles in pseudobulk analysis (Pearson's $r > 0.95$), validating the accuracy and robustness of the snRNA-seq data (*SI Appendix*, Figs. S12 and S13 and Table S22).

To detect IcM populations in snClusters, we reasoned that true IcM cells would exhibit two key characteristics: 1) dynamic changes in their proportional abundance across developmental stages, reflecting activation and subsequent differentiation; and 2) transcriptional signatures of hormone signaling pathways, particularly auxin and cytokinin receptor modules, consistent with meristematic activation and regional identity (Fig. 3*F* and *SI Appendix*, Table S23). SnCluster 2 showed a 54.3% decrease from the ID to RD stage and a further 95.2% drop by RE (two-way ANOVA, Tukey's test, $P = 0.044$), indicating early activation followed by a rapid decline. In contrast, snCluster-1 cells showed a 2.85-fold average increase in cell number from the ID to RE stage (*SI Appendix*, Table S24), exhibiting a proliferative trajectory inverse to snCluster-2 cells (Pearson's $r = -0.997$, $P = 0.045$) (Fig. 3*F* and *SI Appendix*, Table S25). Next, we surveyed gene expression profiles within nine hormone-related pathways (Fig. 3*G* and Dataset S1). Notably, snClusters 2, 7, and 9 presented inverse auxin receptor gradients compared with snCluster-1, suggesting that hormonal regulation plays a crucial role in orchestrating the functional specialization of key cell populations in the IcM region (Fig. 3*G* and *SI Appendix*, Fig. S14). Therefore, subsequent functional analyses targeted snClusters 2, 7, and 9 as representative IcM candidate populations.

Integrated Annotation of IcM Cell Populations. To identify key snClusters (snClusters 2, 7, and 9), we employed an integrated annotation strategy, including functionally validated genes, GO enrichment analysis, orthologous single-cell marker genes, spCluster-enriched genes, robust cell type decomposition (RCTD)-based spatial localization, and ISH experiments. Specifically, these snClusters exhibited increased expression of ERECTA (ER) family genes, including *ER*, *ERECTA-LIKE 1* (*ERL1*), and *ERECTA-LIKE 2* (*ERL2*), which are core regulators of stem cell homeostasis (28–30) (Fig. 4*A* and *SI Appendix*, Fig. S15 and Table S26). GO enrichment analysis revealed a significant association with biological processes such as "DNA replication initiation" and "cell division" (FDR, $P < 0.01$), consistent with active proliferative and meristematic states

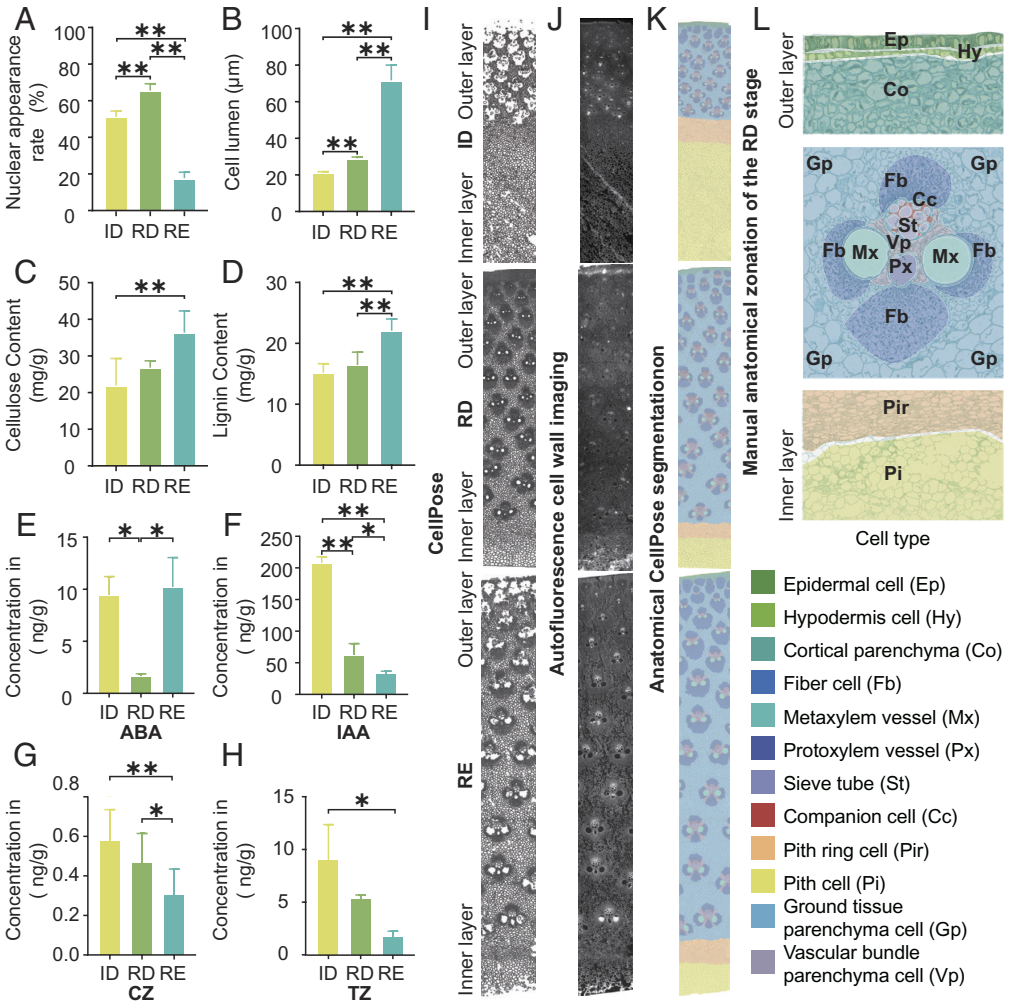

Fig. 2. Anatomical and biochemical characteristics of IcM regions across developmental stages. (*A–D*) Quantification of nuclear density, cell lumen diameter, and cellulose and lignin contents. (*E–H*) LC–MS-based phytohormone profiling of abscisic acid (ABA), indole-3-acetic acid (IAA), cis-zeatin (CZ), and trans-zeatin (TZ). Significance: $^{*}P < 0.05$, $^{**}P < 0.01$. (*I*) Autofluorescence imaging (350 to 400 nm) visualizing cell wall contours for anatomical characterization. (*J*) CellPose-based automated segmentation for high-resolution cell identification. (*K*) Manual classification of anatomical cell types from segmentation results, with color-coded annotations. (*L*) Manual anatomical zonation of the RD stage classified 12 distinct cell types, including epidermal (Ep), hypodermal (Hy), and cortical parenchyma (Co). Vascular core: fiber (Fb), ground tissue parenchyma (Gp), companion cells (Cc), protoxylem (Px), vascular bundle parenchyma (Vp), sieve tubes (St), and metaxylem (Mx). Additionally, the pith region was further divided into the pith ring (Pir) and pith cells (Pi).

(*SI Appendix*, Fig. S16 and Dataset S2). Moreover, orthologous meristem marker genes from *Arabidopsis thaliana* and maize SAMs were highly expressed in these snClusters (31) (Fig. 4*A* and *SI Appendix*, Fig. S17 and Dataset S3). Spatial validation with ISH confirmed the localization patterns predicted by the spatially enriched genes defined from spatial transcriptomics and RCTD-based mapping (Fig. 4 *B–G* and *SI Appendix*, Fig. S18). Thus, this integrative approach enabled the robust annotation of snClusters 2, 7, and 9 as IcM cell populations with high proliferative activity and spatially defined meristematic identities.

Finally, we classified the 13 identified snClusters into 11 distinct functional cell types. In addition to IcM cells (snClusters 2, 7, and 9), the remaining snClusters were annotated as follows: fiber (Fb) cells (snCluster-0), ground tissue parenchyma (Gp) cells (snCluster-1), photosynthetic (Ps) cells (snCluster-3), pith (Pi) cells (snCluster-4), cortex (Co) cells (snCluster-5), protoxylem vessel (Px) cells (snCluster-6), vascular bundle parenchyma (Vp) cells (snCluster-8), companion (Cc) cells (snCluster-10), sieve tube (St) cells (snCluster-11), and metaxylem vessel (Mx) cells (snCluster-12) (*SI Appendix*, Figs. S15–S19 and Tables S26 and S27 and Datasets S2 and S3). To support dynamic data exploration and visualization, we developed an interactive web atlas (https://db.cngb.org/stomics/datasets/STDS0000377), allowing users to query snCluster and spCluster assignments, key gene expression patterns, marker genes, and other transcriptomic features. Additionally, a comparison of cell type annotations derived from anatomical, snRNA-seq, and spatial transcriptomic data demonstrated a high degree of concordance, validating the robustness of our classification and providing a comprehensive cell type reference for the IcM region (Fig. 3*D*). Interestingly, spatial visualization with the expression of spatially enriched genes and RCTD-based mapping revealed that IcM cells are primarily localized within the Gp regions, highlighting their positional specificity within the tissue architecture (Fig. 4 *B–E* and *SI Appendix*, Fig. S18).

Spatial Distribution, Morphology, and Expression Profiles of IcM Cells. To characterize the spatial distribution of IcM cells, ISH analyses revealed that IcM cells adopt a short-columnar morphology and form distinct clusters interspersed within Gp cells (Fig. 5 *A* and *B*). This spatial pattern is consistent with the distribution inferred from the spatial transcriptomic data, further validating the cell type annotations based on spatial transcriptomics. Quantitative measurements revealed that the average lumen diameter of IcM cells was approximately 20 μm,

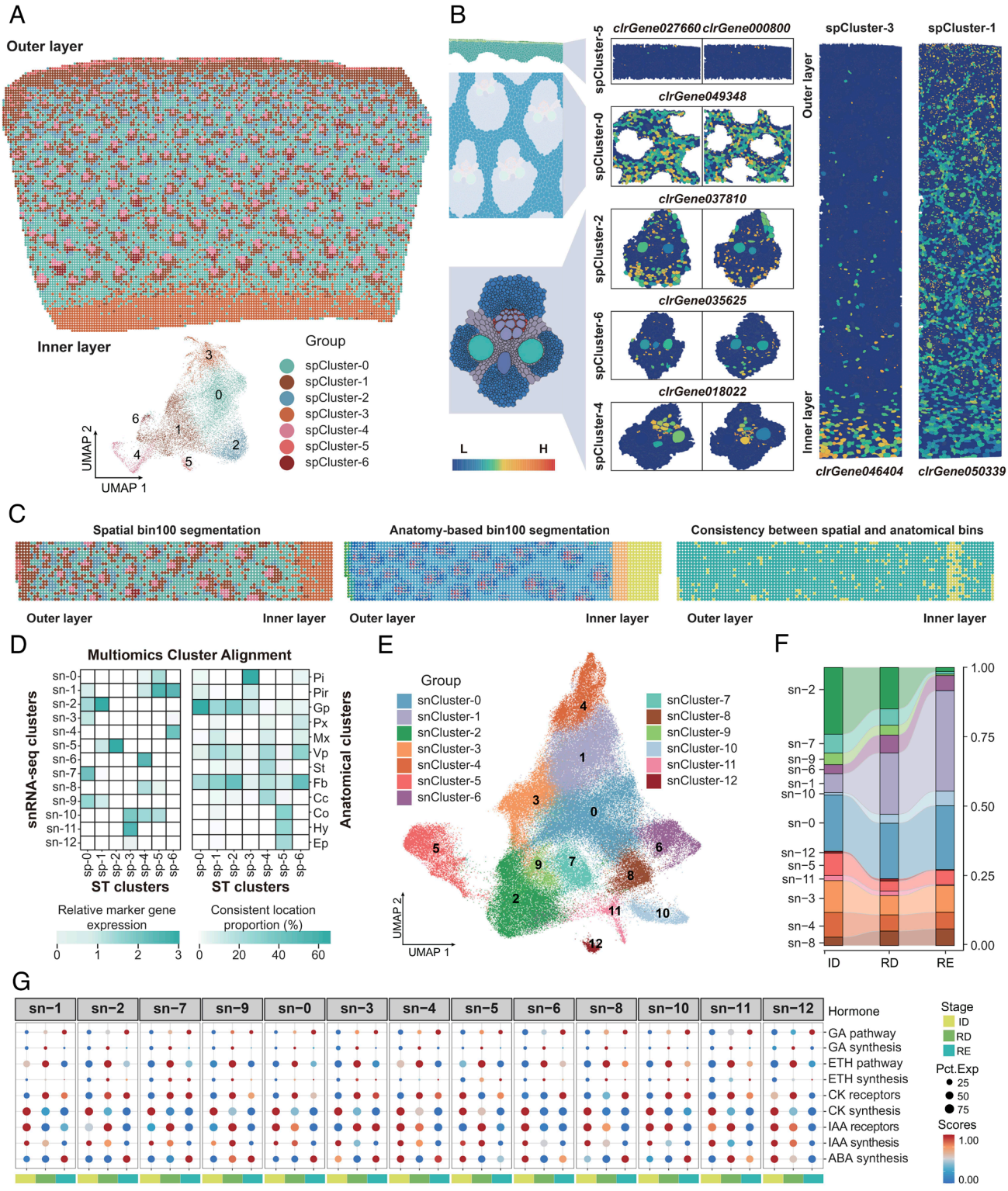

Fig. 3. Transcriptomic classifications identified by snRNA-seq and spatial transcriptomics. (*A*) Spatial cluster (spCluster) distribution from Stereo-seq of an IcM section at the RD stage, with UMAP identifying seven transcriptomic cell populations within the IcM. (*B*) *Left*: anatomically defined cell types. *Right*: spatial expression patterns of selected enriched genes across different spClusters. (*C*) *Left*: spCluster distribution in a local section. Middle: corresponding anatomical zones. *Right*: spatial concordance with anatomical zones (Jaccard index = 88.7%; blue = concordant, yellow = discordant). (*D*) Multiomics alignment: heatmaps showing correspondence between spatial transcriptomic clusters and snRNA-seq clusters (*Left*) and anatomical zones (*Right*). *Left*: mean expression of snRNA-seq marker genes in spatial transcriptomic clusters (row Z-score, only > 0 shown) (detailed in Fig. 4*B*). *Right*: proportion of spatial bins in each spatial transcriptomic cluster overlapping with anatomical zones (detailed in Fig. 3*C*). Color indicates the consistent location proportion. (*E*) Single-nucleus transcriptomic (snRNA-seq) analysis identified 13 distinct single-nucleus clusters (snClusters). (*F*) Changes in snCluster abundance across stages. (*G*) Dot plot of hormone-related gene expression across snClusters (color: normalized expression, size: percentage of expressing cells).

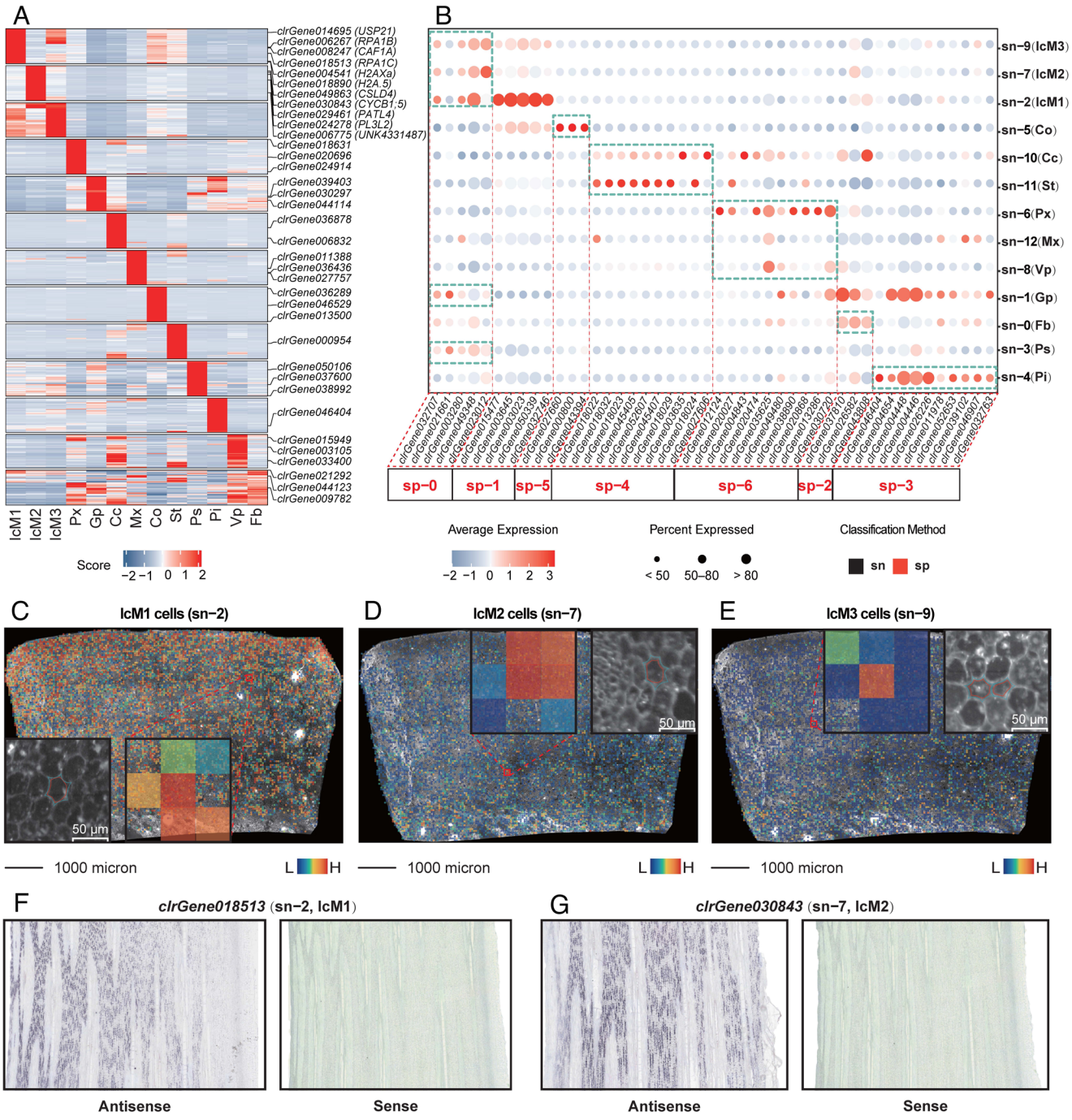

Fig. 4. Annotations and spatial distribution of snRNA-seq-defined cell types. (*A*) Heatmap of Z score–normalized expression for the top 50 marker genes across 13 snClusters; key markers annotated on the *Right*. (*B*) Bubble plot comparing enriched genes for spatial cluster (spCluster, red) annotation with matched snRNA-seq clusters (snCluster, black) (*SI Appendix*, Figs. S17 and S19). Bubble size: cells expressing (%); color: mean expression level. (*C*–*E*) Spatial mapping of IcM1 (sn-2), IcM2 (sn-7), and IcM3 (sn-9) using RCTD at the RD stage, with magnified views of representative regions (full maps in *SI Appendix*, Fig. S18). (*F* and *G*) ISH validation of IcM subtype markers *clrGene018513* (IcM1) and *clrGene030843* (IcM2). Antisense probes showed distinct signals in corresponding IcM populations; sense probes showed no specific signal. These results support the IcM subtype annotation inferred from Fig. 4*A*.

with significantly smaller lumens observed in the outer region of the culm wall (closer to the epidermal layer) than in the inner region (closer to the pith ring) (paired *t* test, $P < 0.01$) (*SI Appendix*, Fig. S20). A similar pattern was observed in Gp cells, which had a larger average lumen diameter of approximately 30 μm but also displayed significantly reduced lumen sizes in the outer layer relative to the inner layer (paired *t* test, $P < 0.01$) (Fig. 5 *A* and *B* and *SI Appendix*, Fig. S20).

We performed scanning electron microscopy (SEM) on longitudinal sections of mature IcM regions to further characterize the ultrastructural features of IcM and Gp cells. SEM imaging revealed a distinct population of short-columnar IcM cells that were morphologically distinguishable from the surrounding Gp cells (Fig. 5*C*). High-magnification SEM imaging of both longitudinal and transverse sections revealed several defining features of IcM cells, including thinner cell walls, well-defined cell corner domains, and characteristic cell wall invagination patterns, which sharply contrasted with the more turgid morphology of adjacent Gp cells (Fig. 5 *D* and *E*). Furthermore, analysis of transverse sections across developmental stages confirmed that these morphological

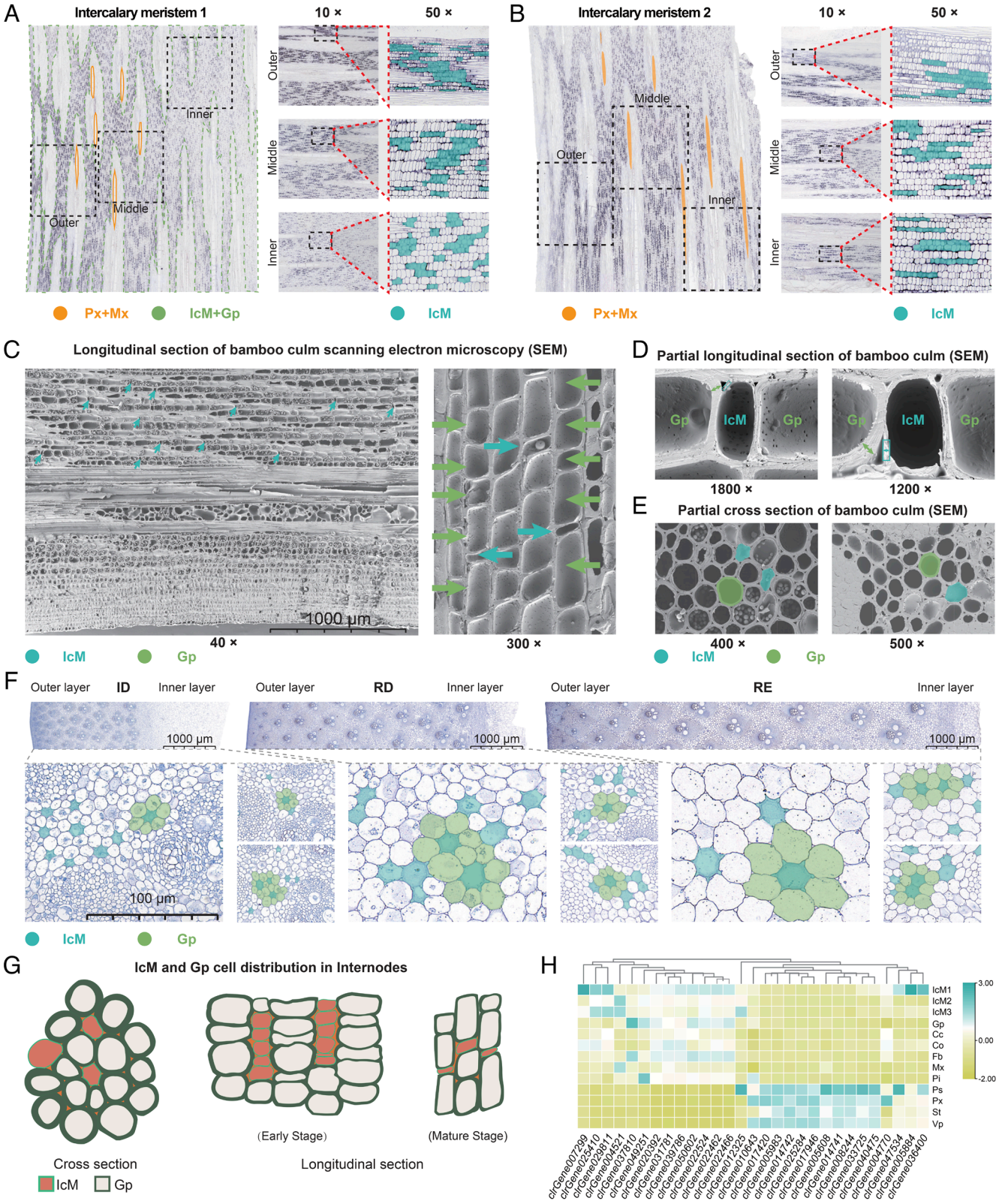

Fig. 5. Morphological characterization of the Moso bamboo IcM. (*A* and *B*) Longitudinal sections of IcM1 and IcM2. Low-magnification images (*Left*) show overall IcM organization; dashed boxes mark regions with 10× and 50× magnifications of outer, middle, and inner layers, highlighting protoxylem (Px), metaxylem (Mx), ground parenchyma (Gp), and IcM cells. (*C*) SEM of longitudinal IcM sections: 40× overview (*Left*) and 300× views (*Right*) revealing IcM and Gp cellular arrangements. (*D* and *E*) Longitudinal and transverse SEM showing fine structural differences between IcM and Gp cells, including wall morphology and intercellular boundaries. (*F*) Transverse sections at low (*Top*) and high (*Bottom*) magnification showing IcM and Gp morphology across developmental stages. (*G*) Schematic cross and longitudinal views of internodes at early and mature stages, illustrating conserved spatial distribution of short-columnar IcM cells among Gp cells. (*H*) Genes enriched in short-columnar cells (spatial transcriptomics) and their expression in snRNA-seq. Four genes identified by spatial transcriptomics analysis showed relatively high expression in IcM1 (sn-2) in snRNA-seq, supporting the cell identity assignment.

characteristics are consistently preserved throughout development (Fig. 5 *F* and *G*), suggesting that the morphological identification of IcM cells represents a fundamental feature of bamboo tissue architecture.

We employed a multiomics approach to identify IcM cells and extracted both short-columnar cells and non-short-columnar cell types from the spatial transcriptomic data to investigate the molecular distinctions among IcM cell subpopulations (see *SI Appendix*, *Materials and Methods*). Short-columnar cells were anatomically segmented (Fig. 5 *F* and *G*), and transcript counts within each segmented boundary were used to generate single-cell expression profiles (*SI Appendix*, Table S28). Transcriptomic profiling revealed that 29 of the top 50 most highly expressed genes were differentially expressed and significantly upregulated in short-columnar cells (FDR, $P < 0.05$) (Fig. 5*H* and *SI Appendix*, Table S28). Functional enrichment analysis further revealed that the "chromosome organization" pathways were significantly enriched, with all four enriched genes exhibiting specific expression in the IcM1 subpopulation (FDR, $P < 0.01$) (Fig. 5*H* and *SI Appendix*, Table S29). Additionally, both snRNA-seq and spatial transcriptomic analyses consistently revealed that IcM cells maintain markedly elevated mitotic activity relative to adjacent Gp cells throughout development. Using cell cycle phase annotation on our snRNA-seq data, 87.0% of IcM nuclei were assigned to S + G2/M phase (indicating elevated proliferative activity) at the RE stage, compared to 14.4% of Gp nuclei (*SI Appendix*, Fig. S21). Complementary RCTD deconvolution of spatial transcriptomics at the RD stage showed 97.6% of transcripts in IcM-enriched spatial bins (spCluster-1) reflected S + G2/M signatures, versus 86.1% in Gp bins (spCluster-0) (*SI Appendix*, Fig. S22). Furthermore, CytoTRACE scoring across all snClusters identified IcM1 cells as having the highest stemness index (*SI Appendix*, Fig. S23). Together, these multimodal analyses demonstrate that IcM populations not only sustain elevated proliferative rates but also harbor greater developmental plasticity compared to neighboring Gp cells.

IcM1 Cells May Represent a Core Population of Stem Cells. To investigate the functional role of IcM1, we analyzed the gene expression profiles associated with stem cell identity and those associated with differentiation potential. CytoTRACE-based analysis revealed that IcM1 cells possessed the highest stemness scores among all identified cell populations (Fig. 6*A* and *SI Appendix*, Fig. S23). Transcriptional profiling of well-established genes associated with stem cell identity, including members of the *WOX* gene family, indicated that most were highly expressed in IcM1 cells (Fig. 6*B* and *SI Appendix*, Table S30). For example, *clrGene008562* (*WOX2*) displayed a progressive increase in expression in IcM1 during the ID and RD phases, supporting its potential role in the maintenance of stem cell identity (Fig. 6*B*). To further elucidate the identity of IcM1 cells, we compared the transcriptomic profiles of the IcM and SAM, which represent the two principal meristem types in plants (Fig. 6 *C* and *D*). IcM1 cells displayed a stronger correlation with the procambium-enriched domain (PED), which ranked highest among all 14 SAM clusters (*SI Appendix*, Table S31). The PED is a specialized SAM subdomain known for its relatively high differentiation capacity (4) (Fig. 6*D* and *SI Appendix*, Fig. S24). Together, these findings suggest that IcM1 shares key molecular characteristics with PED cells and functions as a population with strong stem cell identity, responsible for maintaining meristematic capacity and coordinating differentiation within the IcM region.

To elucidate the mechanisms governing IcM1, we compared transcriptomic profiles spanning the major developmental phase from early development to maturation. IcM1 cells showed the strongest correlation with early-stage developmental transcriptomes (Pearson's $r = 0.80$), which progressively decreased during maturation (Pearson's $r = 0.72$) (Fig. 6*E* and Dataset S4). Additionally, we conducted differential gene expression and chromatin accessibility analyses across IcM cell populations. The "cell differentiation" pathway was significantly enriched in gene sets specific to both IcM1 and IcM2 (FDR, $P < 0.01$) (Fig. 6*F* and *SI Appendix*, Fig. S25 and Table S32). Within the enriched pathway, we then focused on *clrGene008562*, a homolog of *WOX2*, a known regulator of early cell fate determination in *Arabidopsis thaliana* (32, 33) (*SI Appendix*, Figs. S26 and S27 and Tables S33–S35). Expression of the *WOX2* homolog was highly specific to the IcM1 subpopulation, as demonstrated by both snRNA-seq and spatial transcriptomics showing enrichment in short-columnar cells (Fig. 6*G* and *SI Appendix*, Fig. S28). This spatial localization was consistent with anatomically defined IcM regions (Fig. 6*G*). Additionally, although IcM1 cells represented at least 15.5% of all cells at the ID and RD stages, they accounted for up to 67% of total *WOX2* transcripts (*SI Appendix*, Fig. S28), revealing marked transcriptional dominance. Consistent with this, bulk ATAC-seq data exhibited a prominent accessibility peak at the *WOX2* promoter during these same stages (Fig. 6*H*, *SI Appendix*, Tables S36 and S37), suggesting that the observed chromatin accessibility signal likely originates from this specific cell type. Taken together, these findings support a key role for IcM1 in maintaining stem cell identity and initiating early differentiation in the developing IcM region.

We performed overexpression assays in a bamboo-derived callus culture system to characterize *clrGene008562* function. Compared with control cultures, calli overexpressing *clrGene008562* showed significant increases in both proliferation and differentiation capacities (paired *t* test $P < 0.01$), as evidenced by a larger callus size and a greater proportion of differentiated areas (Fig. 6 *I* and *J*). These phenotypic changes were reproducible across three independent biological replicates, supporting the conserved role of *clrGene008562* in promoting callus expansion and differentiation.

Deciphering the Developmental Bifurcation of IcM1: Balancing Maintenance and Differentiation. To elucidate the developmental dynamics of IcM1 and distinguish between the maintenance of stem cell identity and the initiation of differentiation, we reconstructed its pseudotime trajectory and analyzed the transcriptional signatures of cell-cycle-related genes (*SI Appendix*, Fig. S29 *A–D*). Pseudotime analysis revealed two distinct developmental branches: i) differentiation toward Gp cells through an intermediate IcM-to-Gp transitional state (State 2/4) and ii) maturation into a stabilized yet undifferentiated IcM-to-mature state (State 1) (*SI Appendix*, Figs. S29*C* and S30). IcM3 cells initially occupied a position between IcM1 and IcM2, suggesting a transient intermediate role in this trajectory (*SI Appendix*, Fig. S29*B*). Additionally, IcM-specific gene expression profiling revealed that the IcM1–3 subpopulations corresponded to distinct phases of the cell cycle: IcM1 was predominantly associated with S phase (DNA synthesis), IcM3 with G2 phase (premitotic), and IcM2 with M phase (mitosis) (34, 35) (*SI Appendix*, Fig. S29*D* and Table S38). The sequential expression of cell-cycle-related genes across IcM1–3 suggests that these subpopulations may reflect distinct cell cycle phases.

To further explore the dual regulatory strategy of IcM1 cells, we identified four differentiation-associated gene modules along the pseudotime differentiation trajectory clusters (DTClusters) (Dataset S5). The gene modules associated with DTCluster-2 were enriched for pathways involved in cell cycle regulation and stress

adaptation, including core proliferation regulators such as *CDKB2-1* (*clrGene047641*) and *CYCB1-5* (*clrGene030843*), which drive active cell division. This module also featured *WRKY19* (*clrGene012727*) and *GRP5* (*clrGene026677*), which are involved in environmental response pathways, suggesting their potential roles in coordinating stress signaling with the maintenance of stem cell identity in IcM1 cells (*SI Appendix*, Fig. S29*E* and Table S39). Branch-dependent gene analysis further resolved gene modules associated with two intermediate transitional states: i) DTCluster-3, the associated modules were related to environmental adaptation and included transcriptional regulators such as *NAC71* (*clrGene038758*) and *RAP2-4* (*clrGene011271*), which may mediate adaptation-driven differentiation in response to external stimuli. ii) DTClusters-4, this gene module supported core cellular activity and early maturation, and included key genes for ribosome biogenesis, such as translation initiation factor *EIF6* (*clrGene038048*) and ribosomal proteins like *RPL10-2* (*clrGene036078*), and *RPS10-1* (*clrGene032794*). These components are associated with stress adaptation, hormone signaling, and the gradual loss of meristematic potential (*SI Appendix*, Fig. S29*E* and Table S39). Additionally, terminal differentiation is primarily regulated by the DTCluster-1 module, which contains hormone and stress-responsive regulators such as *ERF1* (*clrGene028219*) and *GA2ox3* (*clrGene002384*), representing ethylene and gibberellin signaling components, respectively (*SI Appendix*, Fig. S29*E* and Table S39).

Furthermore, we performed high-dimensional weighted gene coexpression network analysis (hdWGCNA) to elucidate the regulatory mechanism guiding IcM1 fate specification (36) (*SI Appendix*, Figs. S29*F* and S31). This analysis identified two functionally distinct coexpression modules associated with the divergent differentiation trajectories of IcM1 cells. The IcM1-to-Gp transition was associated with the pink module (DTCluster-3), which is likely involved in regulating cell cycle progression and differentiation. This module included key transcriptional regulators such as CPP (*clrGene042910* and *clrGene036810*) and E2F/DP (*clrGene026741*) (*SI Appendix*, Fig. S29*G* and Tables S40 and S41 and Dataset S6). In contrast, the maturation of IcM1 cells toward a nonproliferative, adaptive state was associated with the brown module (DTCluster-4), which potentially mediates growth-defense trade-offs during developmental adaptation. This module contained stress-responsive and developmental regulators, including ERF (*clrGene006464*), LBD (*clrGene010181*), and SBP (*clrGene040372*) (*SI Appendix*, Fig. S29*H* and Tables S40 and S41 and Dataset S6). Together, these findings delineate a bifurcated transcriptional framework in which IcM1 cells gradually commit to distinct developmental fates through distinct molecular programs, ultimately differentiating into either specialized Gp cells or adaptive, mature-oriented IcM1 derivatives.

Discussion

This study investigated IcM-driven rapid internode elongation in Moso bamboo (*P. edulis*) and presented an updated high-quality, chromosome-level genome assembly (Fig. 1). By integrating snRNA-seq, spatial transcriptomics, ATAC-seq, and high-resolution anatomical profiling, we achieved a detailed characterization of IcM region cell types in a plant system (Fig. 1). We systematically delineated the morphological features, spatial distribution, and developmental trajectories of IcM cells, identified key regulatory factors, and reconstructed the regulatory networks that govern the balance between proliferation and differentiation (Fig. 5 and *SI Appendix*, Fig. S29). Additionally, we developed an interactive multiomics data visualization platform (https://db.cngb.org/stomics/datasets/STDS0000377), enabling dynamic exploration of single-cell datasets and serving as a foundational resource for constructing cell atlases in bamboo and other Poaceae species. In summary, this work establishes a framework for spatial single-cell multiomics in nonmodel plants and provides critical insights into the molecular mechanisms underlying rapid growth in monocots. This study also lays both a conceptual and technological foundation for genetic improvement, growth regulation, and molecular breeding in related crops, offering significant theoretical and practical value.

To achieve robust and accurate cell type classification in the IcM region, we established an integrated analytical framework that combines anatomical atlases, snRNA-seq, and spatial transcriptomics. While Stereo-seq provides valuable spatial transcriptomic resolution, it currently has limitations in distinguishing small or closely associated cell types (e.g., sieve tubes and companion cells) (Fig. 3*A*). In contrast, snRNA-seq demonstrated higher sensitivity and resolution in capturing transcriptomic signatures at the single-cell level, although some cell types (e.g., parenchyma cells) remain difficult to annotate owing to the lack of well-defined marker genes (Fig. 4*A* and *SI Appendix*, Tables S19 and S26 and Datasets S2 and S3). To overcome the complementary limitations of each technology, we developed an integrated framework in which the anatomical atlas served as a structural reference, snRNA-seq resolved the transcriptional heterogeneity, and spatial transcriptomics refined and validated the spatial annotation. This strategy enabled the construction of a multidimensional, high-precision cell classification system in the IcM region. Additionally, we developed an innovative, label-free, high-resolution cell contour segmentation method using intrinsic cell wall autofluorescence combined with machine learning algorithms, achieving accurate single-cell-level segmentation and spatial localization (Fig. 2 *I*–*K*). In addition to bamboo, this integrated multiomics pipeline provides a powerful and adaptable framework for cell atlas construction and developmental studies in other complex plant tissues.

Owing to their transient activity, rapid differentiation, and discrete embedding within mature tissues, IcM cells have historically been difficult to localize and characterize (37). By integrating spatial transcriptomics and snRNA-seq, we identified IcM cells as short-columnar cell clusters interspersed among Gp cells (Figs. 4 and 5). ISH and scanning electron microscopy (SEM) further confirmed that, although IcM cells share parenchymatous characteristics, they are morphologically distinct from surrounding Gp cells (Fig. 5 *C*–*G*). Additionally, two primary hypotheses have been proposed regarding the developmental origin of IcM cells: One suggests derivation from the SAM, whereas the other proposes the reactivation of mitotic capacity in differentiated tissues (38, 39). Our data, including the high expression of stem cell maintenance genes in the IcM and transcriptional similarity between IcM cells and the procambium-enriched domain (PED) of the SAM, support a SAM-origin model (Fig. 6 *B* and *D* and *SI Appendix*, Tables S26 and S29). Based on these insights, we propose a spatiotemporal developmental model in which IcM cells originate from the SAM and are initially distributed throughout the internode. These cells follow a top–down maturation gradient: Apical IcM cells exit the proliferative state earlier and transition into elongation-dominant Gp cells, whereas basal IcM cells maintain their proliferative and differentiation potential for a prolonged period. As development progresses, residual IcM cells persist as active, discrete clusters within the Gp regions, gradually losing their stem-like identity. This model provides a conceptual framework for understanding the spatial organization and

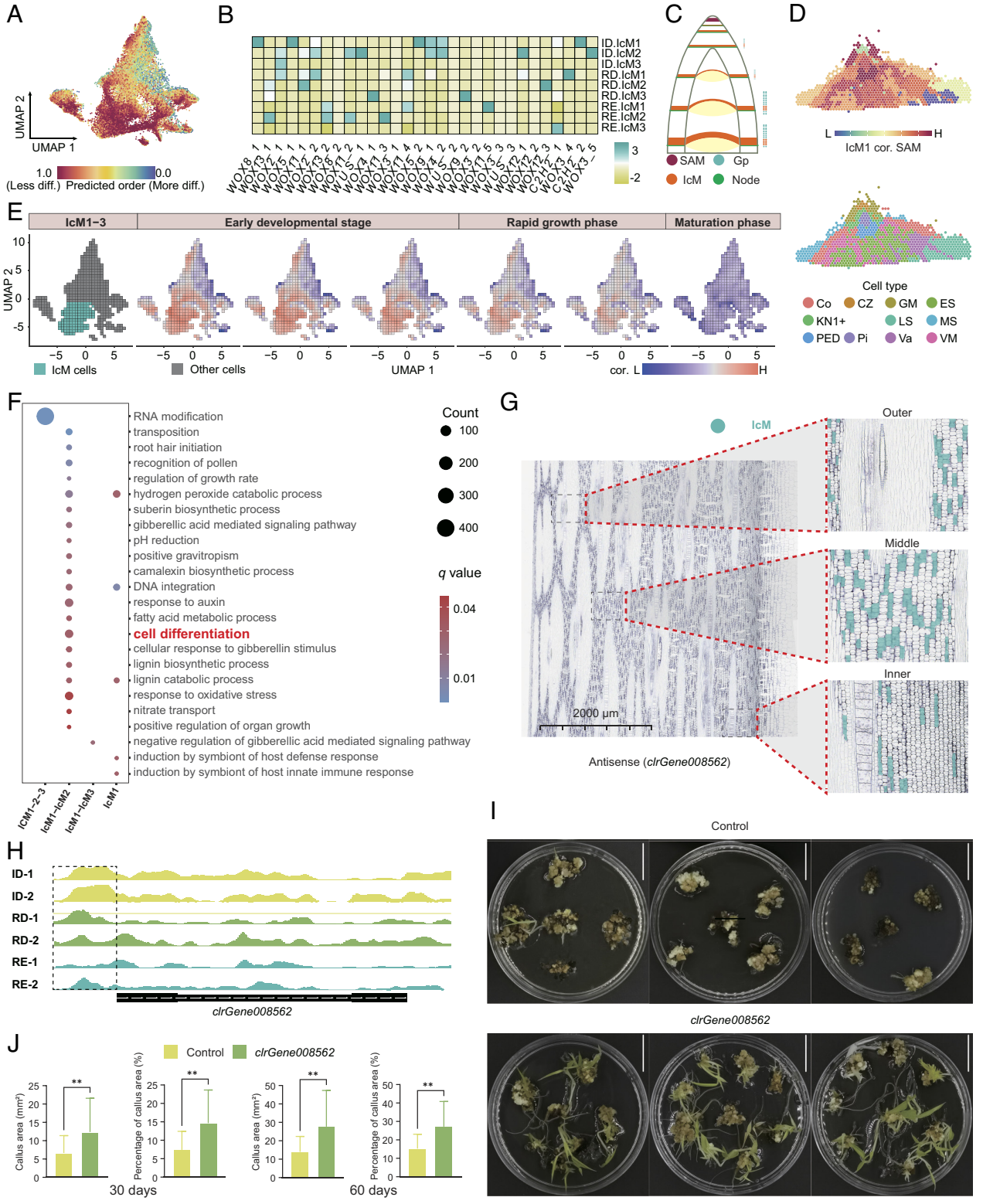

Fig. 6. The stem cell identity of IcM cells and the functional role of the *WOX2* homolog in Moso bamboo. (*A*) UMAP colored by CytoTRACE predicted differentiation potential (red: stem-like, blue: differentiated); IcM1–3 showed higher scores, indicating stronger stem cell identity. (*B*) Heatmap showing the expression of stem cell identity–related genes across the ID, RD, and RE stages. (blue: high expression, yellow: low expression). (*C*) Schematic representation of the shoot apical meristem (SAM), IcM, Gp (ground parenchyma), and nodes. (*D*) Hexbin plot (*Left*) showing gene expression correlation between IcM and SAM cell types (red: high expression, blue: low expression); *Right*: spatial distribution of SAM cell types. (*E*) Compared transcriptomic profiles across developmental stages from early growth to maturation. The panel series shows that IcM1 cells (cyan) presented the strongest correlation with early-stage developmental transcriptomes (Pearson's $r > 0.8$), which progressively decreased during maturation (Pearson's $r > 0.7$). (*F*) Dot plot showing enrichment of "cell differentiation" GO term in IcM1 and IcM2 (FDR $P < 0.01$; size: gene number, color: significance). (*G*) The spatial expression of *clrGene008562* resembles the anatomical pattern of IcM cells. ISH revealed that *clrGene008562* is specifically expressed in short, continuous cell files embedded within Gp tissues, which is consistent with the morphological distribution of IcM cells across the outer, middle, and inner layers. (*H*) ATAC-seq revealed peak accessibility of *clrGene008562* (*WOX2* homolog) during ID stages, suggesting a role in differentiation initiation. (*I*) Overexpression of *clrGene008562* in *Dendrocalamus brandisii* callus promoted proliferation and shoot primordia formation compared with control. (*J*) Quantification at 30 and 60 d postinduction showed significantly increased callus growth and differentiation in OE lines (paired *t* test, $P < 0.01$).

developmental plasticity of IcM cells and provides a mechanistic basis for exploring internode elongation and stem growth regulation in bamboo and other Poaceae species.

Materials and Methods

IcMs were sampled at three developmental stages–initiation of cell division (ID), rapid division (RD), and rapid elongation (RE)–from a single clonal Moso bamboo shoot (*P. edulis*) cultivated at the ICBR Taiping Experimental Center in Huangshan, Anhui Province, China (30°21′ N, 118°01′ E). A de novo chromosome-level assembly was generated from this same individual using PacBio continuous long reads and Hi-C scaffolding. The assembly served as the reference for all multiomics analyses. Multiomics profiling comprised bulk RNA-seq (three replicates per stage), bulk ATAC-seq (two replicates), single-nucleus RNA-seq (two replicates), and high-resolution Stereo-seq spatial transcriptomics (three sections). Data processing and cell type annotation employed established bioinformatics pipelines. Complementary analyses included histological staining, scanning electron microscopy, 3D X-ray CT reconstruction, cellulose/lignin colorimetric quantification, and UPLC–MS/MS phytohormone profiling. Additionally, we used callus as recipient tissue for an *Agrobacterium*-mediated transformation of a *WOX*-overexpression construct, following standard infection, selection, and differentiation procedures. Detailed methodologies are available in *SI Appendix, Materials and Methods*.

Data, Materials, and Software Availability. All sequencing data generated in this study are publicly accessible through the following repositories: 1) Bulk datasets, including bulk RNA-seq and bulk ATAC-seq datasets, are available through the National Center for Biotechnology Information (NCBI) Sequence Read Archive (SRA) under accession numbers PRJNA1181664 (40) and PRJNA1178344 (41). 2) Whole-genome sequencing data, including PacBio long reads, short reads, and Hi-C data, as well as snRNA-seq and Stereo-seq datasets, have been deposited in the Genome Sequence Archive (GSA) under accession number CRA023164 (42) and in the China National GenBank (CNGB) under accession number CNP0006948 (43). Additionally, our specialized online resource is operational and publicly accessible at https://db.cngb.org/stomics/datasets/STDS0000377 (44). The customized codes used in this study have been deposited in GitHub (https://github.com/ZhaoGroupLab/ST) (45). The raw data underlying all the main and supplementary figures are provided in the Source Data file associated with this publication (*SI Appendix*, Datasets S7 and S8).

ACKNOWLEDGMENTS. This work received financial support from the National Natural Science Foundation of China (32430072 to H.Z.), the National Key Research and Development Program of China (2021YFD2201000 to H.Z.), the National Natural Science Foundation of China (32271975 to H.Z.), and the Research and Demonstration of Key Technologies for "Bamboo as Substitutes for Plastic" in Pilot Member States of the International Bamboo and Rattan Organization. We thank the Plant SpatioTemporal Omics Consortium (STOC Plant) for their support.

Author affiliations: [a]Institute of Gene Science and Industrialization for Bamboo and Rattan Resources, International Centre for Bamboo and Rattan, Beijing 100102, China; [b]Key Laboratory of National Forestry and Grassland Administration/Beijing for Bamboo and Rattan Science and Technology, Beijing 100102, China; [c]Beijing Genomics Institute Research, Beijing 102601, China; [d]Beijing Genomics Institute Research, Shenzhen, Guangdong 518083, China; [e]State Key Laboratory of Genome and Multi-omics Technologies, Beijing Genomics Institute Research, Shenzhen 518083, China; [f]State Key Laboratory of Crop Genetics and Germplasm Enhancement and Utilization, Bioinformatics Center, Academy for Advanced Interdisciplinary Studies, Nanjing Agricultural University, Nanjing, Jiangsu 210000, China; [g]Institute of New Bamboo and Rattan Based Biomaterials, International Centre for Bamboo and Rattan, Beijing 100102, China; and [h]Shenzhen Key Laboratory of Transomics Biotechnologies, Beijing Genomics Institute Research, Shenzhen 518083, China

Author contributions: X.L., H.Y., and H.Z. designed research; J.L., Y.W., and H.Z. performed research; X.W., Z.F., and H.Z. contributed new reagents/analytic tools; N.Q., S.L., L.S., C.C., W.L., P.B., B.C., H.Z., J.G., Y.H., Z.F., and Y.W. analyzed data; and X.L. and H.Z. wrote the paper.

1. P. Awale, P. McSteen, Hormonal regulation of inflorescence and intercalary meristems in grasses. *Curr. Opin. Plant Biol.* **76**, 102451 (2023).
2. K. Nagai, Y. Niimi, M. Ohsato, M. Ashikari, Developmental dynamics of intercalary meristem and pith cavity in rice stems. *Rice* **18**, 18 (2025).
3. F. Wang *et al.*, ZmTE1 promotes plant height by regulating intercalary meristem formation and internode cell elongation in maize. *Plant Biotechnol. J.* **20**, 526–537 (2022).
4. J. Guo *et al.*, Spatiotemporal transcriptome atlas reveals gene regulatory patterns during the organogenesis of the rapid growing bamboo shoots. *New Phytol.* **244**, 1057–1073 (2024).
5. B. Wang, S. Smith, J. Li, Genetic regulation of shoot architecture. *Annu. Rev. Plant Biol.* **69**, 437–468 (2018).
6. J. Oliver *et al.*, The AGCVIII kinase Dw2 modulates cell proliferation, endomembrane trafficking, and MLG/xylan cell wall localization in elongating stem internodes of *Sorghum bicolor*. *Plant J.* **105**, 1053–1071 (2021).
7. M. Neumann *et al.*, A 3D gene expression atlas of the floral meristem based on spatial reconstruction of single nucleus RNA sequencing data. *Nat. Commun.* **13**, 2838 (2022).
8. C. Wang, X. Yang, G. Li, Molecular insights into inflorescence meristem specification for yield potential in cereal crops. *Int. J. Mol. Sci.* **22**, 3508 (2021).
9. Z. Peng *et al.*, Transcriptome sequencing and analysis of the fast growing shoots of moso bamboo (*Phyllostachys edulis*). *PLoS One* **8**, e78944 (2013).
10. W. Liese, T. Tang, "Properties of the bamboo culm", in *Bamboo*, W. Liese, M. Köhl, Eds. (Springer Cham, Switzerland, 2015), pp. 227–256.
11. M. Chen *et al.*, Rapid growth of moso bamboo (*Phyllostachys edulis*): Cellular roadmaps, transcriptome dynamics, and environmental factors. *Plant Cell* **34**, 3577–3610 (2022).
12. Z. Peng *et al.*, Genome-wide characterization of the biggest grass, bamboo, based on 10,608 putative full-length cDNA sequences. *BMC Plant Biol.* **10**, 116 (2010).
13. G. Tao *et al.*, Multi-omics analysis of cellular pathways involved in different rapid growth stages of moso bamboo. *Tree Physiol.* **40**, 1487–1508 (2020).
14. R. Gamuyao *et al.*, Hormone distribution and transcriptome profiles in bamboo shoots provide insights on bamboo stem emergence and growth. *Plant Cell Physiol.* **58**, 702–716 (2017).
15. Y. Li *et al.*, Transcriptome and miRNAome analysis reveals components regulating tissue differentiation of bamboo shoots. *Plant Physiol.* **188**, 2182–2198 (2022).
16. X. Luo *et al.*, Abscisic acid inhibits primary root growth by impairing ABI4-mediated cell cycle and auxin biosynthesis. *Plant Physiol.* **191**, 26–279 (2023).
17. H. Zhang *et al.*, ABA promotes quiescence of the quiescent centre and suppresses stem cell differentiation in the Arabidopsis primary root meristem. *Plant J.* **64**, 764–774 (2010).
18. Y. Su *et al.*, Integration of pluripotency pathways regulates stem cell maintenance in the *Arabidopsis* shoot meristem. *Proc. Natl. Acad. Sci. U.S.A.* **117**, 22561–22571 (2020).
19. Q. Nguyen, N. Pervolarakis, K. Nee, K. Kessenbrock, Experimental considerations for single-cell RNA sequencing approaches. *Front. Cell Dev. Biol.* **6**, 108 (2018).
20. K. Xia *et al.*, The single-cell stereo-seq reveals region-specific cell subtypes and transcriptome profiling in *Arabidopsis* leaves. *Dev. Cell* **57**, 1299–1310.e4 (2022).
21. H. Zhao *et al.*, Analysis of 427 genomes reveals moso bamboo population structure and genetic basis of property traits. *Nat. Commun.* **12**, 5466 (2021).
22. Y. Hou *et al.*, Haplotype-based pangenomes reveal genetic variations and climate adaptations in moso bamboo populations. *Nat. Commun.* **15**, 8085 (2024).
23. H. Zhao *et al.*, Chromosome-level reference genome and alternative splicing atlas of moso bamboo (*Phyllostachys edulis*). *GigaScience* **7**, giy115 (2018).
24. M. Pachitariu, C. Stringer, Cellpose 2.0: how to train your own model. *Nat. Methods* **19**, 1634–1641 (2022).
25. D. Grosser, W. Liese, On the anatomy of Asian bamboos, with special reference to their vascular bundles. *Wood Sci. Technol.* **5**, 290–312 (1971).
26. W. Liese, "Structure of the internode" in *The Anatomy of Bamboo Culms* (INBAR, Beijing, 1998), pp. 15–90.
27. X. Song *et al.*, Spatial transcriptomics reveals light-induced chlorenchyma cells involved in promoting shoot regeneration in tomato callus. *Proc. Natl. Acad. Sci. U.S.A.* **120**, e2310163120 (2023).
28. M. Chen, R. Wilson, K. Palme, F. Ditengou, E. Shpak, *ERECTA* family genes regulate auxin transport in the shoot apical meristem and forming leaf primordia. *Plant Physiol.* **162**, 1978–1991 (2013).
29. N. Uchida, M. Shimada, M. Tasaka, *ERECTA*-family receptor kinases regulate stem cell homeostasis via buffering its cytokinin responsiveness in the shoot apical meristem. *Plant Cell Physiol.* **54**, 343–351 (2013).
30. N. Uchida, M. Shimada, M. Tasaka, Modulation of the balance between stem cell proliferation and consumption by *ERECTA*-family genes. *Plant Signal. Behav.* **7**, 1506–1508 (2012).
31. Z. He *et al.*, scPlantDB: A comprehensive database for exploring cell types and markers of plant cell atlases. *Nucleic Acids Res.* **52**, D1629–D1638 (2024).
32. A. Haecker *et al.*, Expression dynamics of *WOX* genes mark cell fate decisions during early embryonic patterning in *Arabidopsis thaliana*. *Development* **131**, 657–668 (2004).
33. H. Breuninger, E. Rikirsch, M. Hermann, M. Ueda, T. Laux, Differential expression of *WOX* genes mediates apical-basal axis formation in the *Arabidopsis* embryo. *Dev. Cell* **14**, 867–876 (2008).
34. L. De Veylder, T. Beeckman, D. Inzé, The ins and outs of the plant cell cycle. *Nat. Rev. Mol. Cell Biol.* **8**, 655–665 (2007).
35. R. Sablowski, C. Gutierrez, Cycling in a crowd: Coordination of plant cell division, growth, and cell fate. *Plant Cell* **34**, 193–208 (2022).
36. S. Morabito, F. Reese, N. Rahimzadeh, E. Miyoshi, V. Swarup, hdWGCNA identifies co-expression networks in high-dimensional transcriptomics data. *Cell Rep. Methods* **3**, 100498 (2023).
37. K. Yu *et al.*, Bioenergy sorghum stem growth regulation: intercalary meristem localization, development, and gene regulatory network analysis. *Plant J.* **112**, 476–492 (2022).
38. H. Morinaka, Y. Sakamoto, A. Iwase, K. Sugimoto, How do plants reprogramme the fate of differentiated cells? *Curr. Opin. Plant Biol.* **74**, 102377 (2023).
39. N. Uchida, K. Torii, Stem cells within the shoot apical meristem: identity, arrangement and communication. *Cell. Mol. Life Sci.* **76**, 1067–1080 (2019).

40. X. Yi *et al.*, ATAC-seq data from "Epigenetic regulation and transcriptional divergence drive lignification in rapidly growing Moso bamboo." NCBI BioProject. https://www.ncbi.nlm.nih.gov/bioproject/PRJNA1181664. Deposited 21 August 2025.
41. X. Yi *et al.*, RNA-seq data from "Epigenetic regulation and transcriptional divergence drive lignification in rapidly growing Moso bamboo." NCBI BioProject. https://www.ncbi.nlm.nih.gov/bioproject/PRJNA1178344. Deposited 21 August 2025.
42. N. Qin *et al.*, Data from "Single-nucleus and spatial transcriptomics reveal the cell populations of intercalary meristems in bamboo." Genome Sequence Archive (GSA). https://ngdc.cncb.ac.cn/gsa/search?searchTerm=CRA023164. Deposited 28 February 2025.
43. N. Qin *et al.*, Data from "Single-nucleus and spatial transcriptomics reveal the cell populations of intercalary meristems in bamboo." China National GeneBank DataBase (CNGBdb). https://db.cngb.org/data_resources/project/CNP0006948. Deposited 28 February 2025.
44. N. Qin *et al.*, Data from "Single-nucleus and spatial transcriptomics reveal the cell populations of intercalary meristems in bamboo." STOmicsDB. https://db.cngb.org/stomics/datasets/STDS0000377. Deposited 18 March 2025.
45. N. Qin *et al.*, Data from "Single-nucleus and spatial transcriptomics reveal the cell populations of intercalary meristems in bamboo." GitHub. https://github.com/ZhaoGroupLab/ST. Deposited 4 August 2025.